Supplementary information for

Polymorphous packing of pentagonal nanoprisms

Jules Marcone,[†] Wajdi Chaâbani,[†] Claire Goldmann,[†] Marianne Impéror-Clerc,[†] Doru Constantin,[*,‡] and Cyrille Hamon[*,†]

[†]*Laboratoire de Physique des Solides, CNRS and Université Paris-Saclay, 91400 Orsay, France*

[‡]*Institut Charles Sadron, CNRS and Université de Strasbourg, 67034 Strasbourg, France*

E-mail: constantin@unistra.fr; cyrille.hamon@universite-paris-saclay.fr

Contents

S1 Materials and Methods

Materials. Gold chloride trihydrate ($HAuCl_4 \cdot 3H_2O$ ≥99.9%, silver nitrate ($AgNO_3$ >99%), sodium borohydride ($NaBH_4$ ≥96%), trisodium citrate dihydrate (99%), L-ascorbic acid (AA, ≥99%), CTAC (25 wt % in H_2O), and benzyldimethylhexadecylammonium chloride (BDAC 99%) were purchased from Merck and used without further purification.

Characterization of the NPs. UV/Vis/NIR absorption spectra were collected using a Cary 5000 UV-Vis-NIR. All experiments were carried out at room temperature, using disposable polystyrene cuvettes with optical paths of 1 cm. TEM was performed at IMAGIF (I2BC CNRS, Gif s/Yvette, France) using a JEOL JEM-1400 microscope operating at 120 kV with a filament current of about 55 μA. SEM was performed at the LPS with a Zeiss Supra55VP with an acceleration voltage of 5 keV.

Decahedra synthesis. Gold decahedra were prepared following the procedure of Sánchez-Iglesias et al.[S1]

Seeds. In a 50 mL bottle, 2.65 mL of CTAC (25 wt % in H_2O) and 400 μL of $HAuCl_4$ 25 mM were mixed to 33 mL of water and heated at 30°C for 10 minutes. 4 mL of sodium citrate 50 mM were added and the heating was continued for 30 minutes. Under fast stirring, 1 mL of freshly prepared $NaBH_4$ 25 mM was added, the bottle was closed and put in the oven at 40°C for 5 days.

Growth. At 30°C, 500 μL of $HAuCl_4$ 25 mM were added to 25 mL of BDAC 100 mM, followed by 188 μL of ascorbic acid 100 mM. Under fast stirring, a certain amount of seeds (between 10 μL and 600 μL) was added, and the reaction medium was left under slow stirring at 30°C for 30 minutes. The decahedras were centrifuged at an appropriate speed and washed with CTAC 1 mM.

Concentration measurement. 10 μL of AuDHs were diluted in 2000 μL of water and the absorbance at 400 nm was recorded with a UV-visible spectrometer in order to estimate

the Au^0 concentration.[S2,S3]

NP growth from AuDHs. In a vial, water, CTAC and AuDHs were mixed and heated at 70°C for 5 minutes. Under strong stirring, silver nitrate was added, followed by ascorbic acid, the vial was closed and the reaction medium was heated for 2 hours at 70°C (see fig. S1 for precise quantities). At the end of the synthesis, the UV-visible spectra were recorded and the particles were centrifuged and washed with CTAC 1 mM. 1 mL of water was added, followed by a proper amount of CTAC (25 wt%) to reach an appropriate concentration allowing the purification of the NPs by depletion. The solutions were left overnight to precipitate, the supernatant and the precipitate were separated, analyzed by UV-visible spectroscopy, and the precipitate was washed by centrifugation and redispersed in CTAC 2.5 mM.

Sample	Figure	H_2O (µL)	CTAC 100 mM (µL)	DHs (µL)	$AgNO_3$ 100 mM (µL)	AA (µL)	[CTAC] for purification (mM)
NPs-1	Fig.S5	3500	400	DHs1 : 101 ([Au] = 9.88 mM)	95	76 (500 mM)	100
NPs-2	Fig.S6	3500	400	DHs2 :83.3 ([Au] = 12.0 mM)	20	16 (500 mM)	70
NPs-3	Fig.S7	3500	400	DHs3 :78 ([Au] = 12.8 mM)	10	40 (100 mM)	70
NPs-4	Fig.1-2-3	3500	400	DHs4 :163 ([Au] = 6.13 mM)	20	80 (100 mM)	70
NPs-5	Fig.S8	3500	400	DHs5 :98 ([Au] = 10.2 mM)	10	40 (100 mM)	53

Figure S1: Quantities used for the synthesis of Ag nanoprisms.

NP self-assembly. Supercrystals were formed via evaporation-induced self-assembly of a sessile droplet. In typical conditions, a 10 μL NPs dispersion (40 mM in Au^0 and 2.5 mM CTAC) was drop casted on a Si substrate and dried in a sealed Petri dish, which was loaded with water. This resulted in the slow evaporation of the suspension for about 48 h.

Numerical simulations. Electric near-fields distributions were calculated with finite-difference time-domain (FDTD) methods. In FDTD model, the total-field scattered-field source was used to realize the plane wave incidence. The wavelength range of the simulation is set between 400 nm and 1400 nm. The boundary conditions of the perfectly matched layer were applied, and the three-dimensional sizes were set at $2\mu\text{m} \times 2\mu\text{m} \times 2\mu\text{m}$. A nonuniform mesh with the smallest size of 0.5 nm as well as a perfectly matched boundary was employed in the numerical simulations. The dielectric function of silver and gold were taken from the material database of Palik and Johnson and Christy (provided by FDTD Solutions, Lumerical). The movies of electric field were built using a script in Matlab.

S2 Optimization of the self-assembly conditions of the pentagonal NPs into extended supercrystals

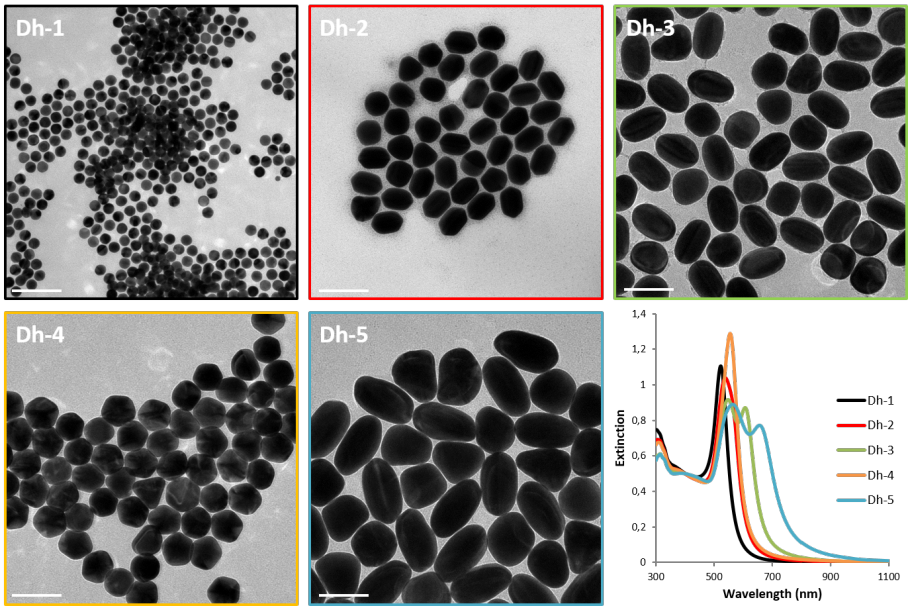

Figure S2: Characterization of the gold decahedral seeds. TEM images of the five decahedral seeds batch: Dh1, Dh2, Dh3, Dh4 and Dh5 used to prepare NPs-1, NPs-2, NPs-3 NPs-4 and NPs-5 respectively. Bottom right: corresponding extinction spectra. Scale bar on all images is 100 nm

Monodisperse silver nanoprisms (NPs) with controllable aspect ratios can be formed by

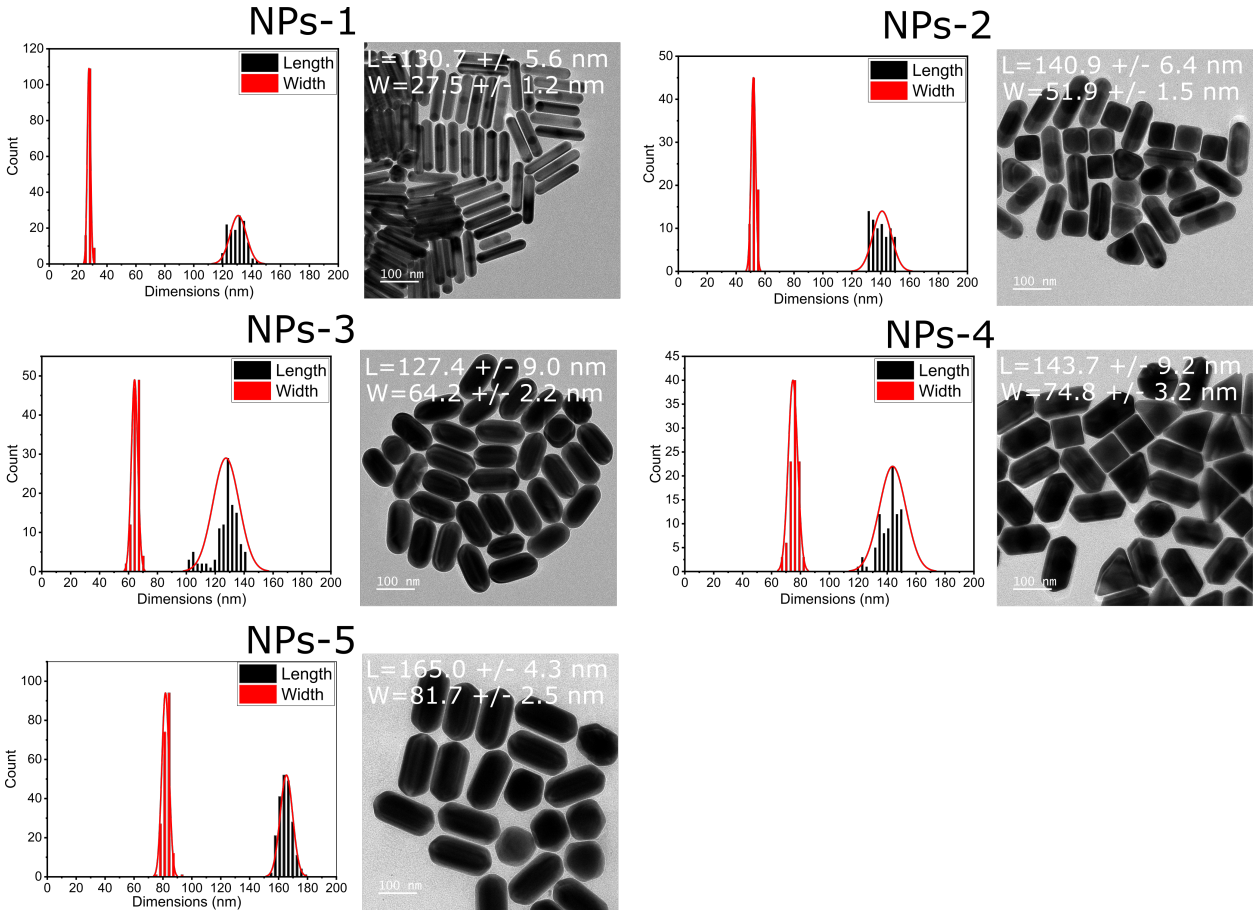

Figure S3: Characterization of the Ag nanoprisms. TEM image and corresponding size distribution histograms. The average size distribution and standard deviation for each batches is indicated on the corresponding TEM images. TEM images have been taken before shape purification.

templated growth from pentatwinned seeds.[S4–S6] In a typical synthesis, the metallic precursor deposits on the tips of the seeds, while the diameter of the NPs remains almost constant over the growth process. Although the length of the NPs can be well controlled by adjusting the amount of metallic precursors, the diameter can only be tuned by using seeds of different dimensions. We tried different pentatwinned seeds (gold bipyramids and decahedra) and choose decahedra because their size can be tuned in a greater range (diameter between 25 and 90 nm) than bipyramids. Figure S2 present some TEM images of the seeds and the corresponding extinction spectra. Five AgNRs batches were prepared from five different decahedra seeds resulting in the samples denoted as NPs-1, NPs-2, NPs-3, NPs-4 and NPs-5

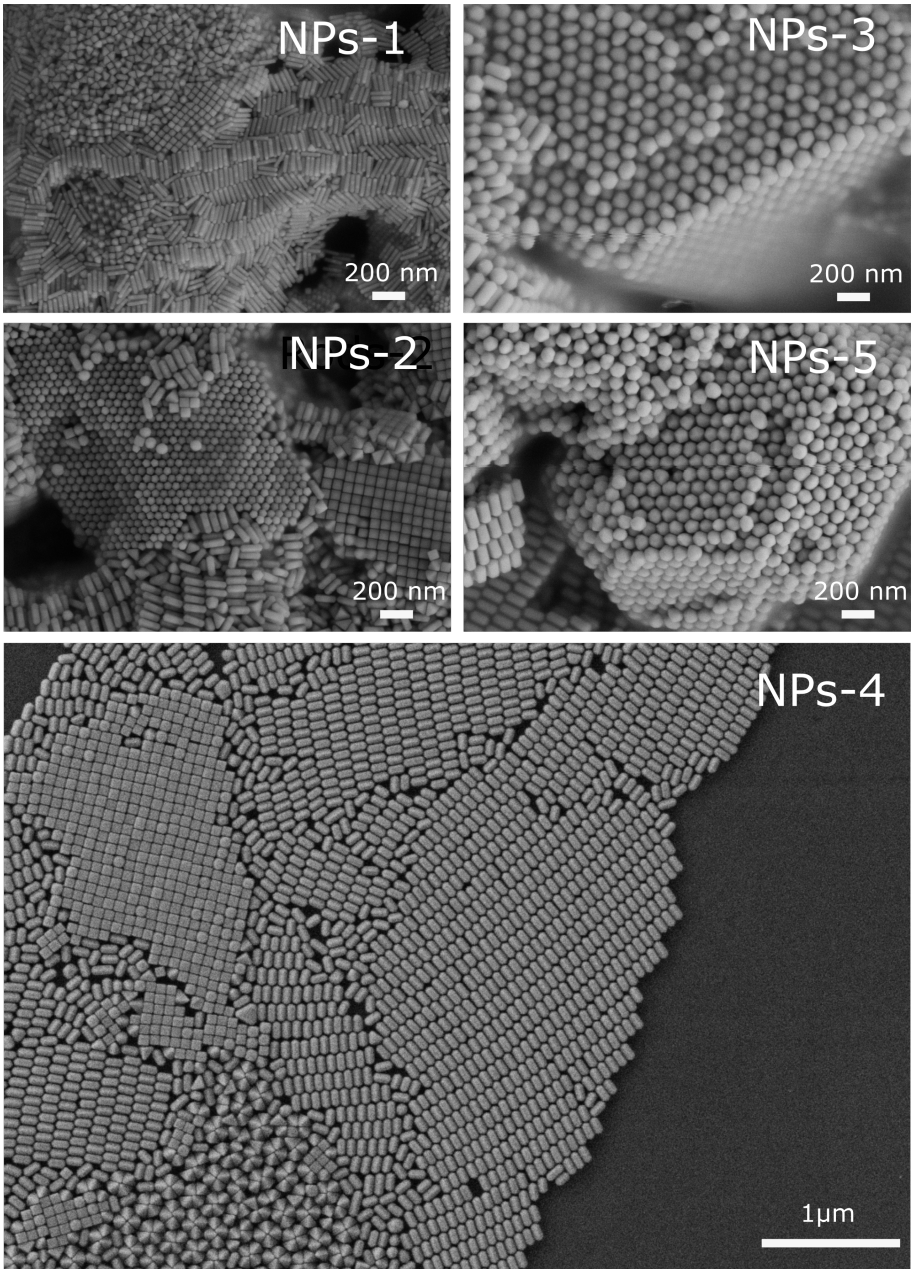

Figure S4: Self-assembly with byproducts. SEM images at high magnification of AgNRs assemblies without preliminary shape purification.

(see Figure S3) Each AgNRs batch was uniform in size, as shown by a relative standard deviation of width below 5%. Self-assembly was conducted by the slow evaporation (over 48 h) of a sessile droplet on a silicon wafer and the nanostructuration was probed by SEM (see Figure S4). Although close-packing was observed in all samples, the extension of the domain was limited to a few micrometers. This is presumably due to the presence of bipyproducts

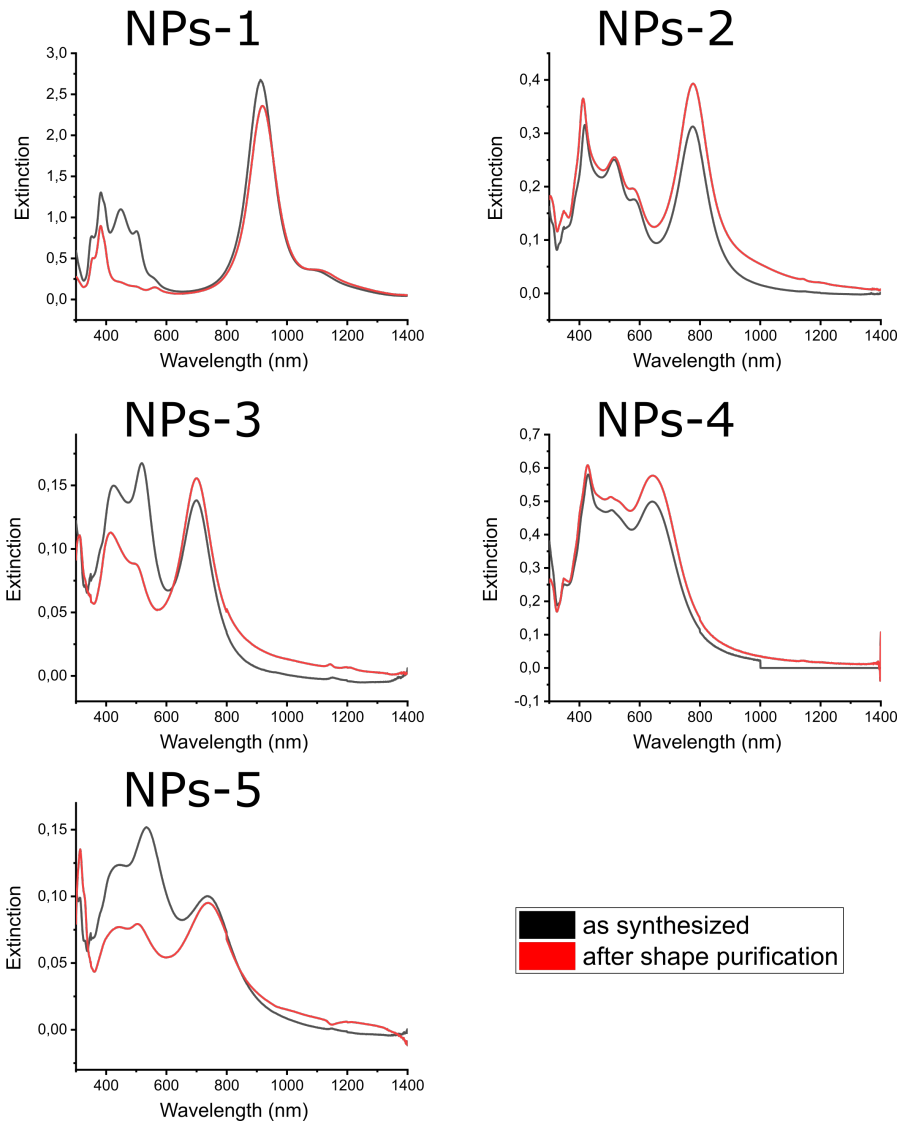

Figure S5: Extinction spectra of the Ag NPs, after synthesis (black) and after shape purification by depletion induced self-assembly.

(triangular right bipyramids, spheroids and cubes), which self assemble in separate domain or within mixed amorphous domains. We therefore purified the suspensions by shape-selective precipitation, using so-called depletion induced self-assembly, in which surfactant micelles (CTAC) induce NPs flocculation by excluded volume interaction.[S7] By this process, NPs featuring a high area of interaction form superstructures that sediment to the bottom of the flask (while the other remains in suspension). After discarding the supernatant, the pellet containing the nanoprisms was redispersed upon dilution. Figure S5 shows the extinction

spectra of the NPs after synthesis and after purification. The longitudinal plasmon band of the NPs remain after purification, while other plasmon bands at high energy (corresponding to the byproducts) are discarded, indicating the success of the shape selection process. Self-assembly was then conducted again and extended monodomains as shown in Figure 1 of the main text and in section S3.[S8,S9] We next analyze the effect of NPs size on the ordering of the SCs. Images of NPs-1 were not analyzed because it was challenging to observe their pentagonal cross section in SEM. Moreover, no extended SCs were observed for NPs-5, presumably because not all byproducts were successfully discarded from the suspension. The width of the Gaussian peaks in the histogram of the α distribution provides a quantitative measure for the orientational order of the pentagons. We determined this parameter (termed "disorientation") for NPs sizes we used in this work. The results for NPs-2, NPs-3 and NPs-4 are shown in Figure S7. We conclude that the orientational order of the pentagons decreases as the objects get smaller, most clearly from 75 to 64 nm. In Figure S8 we show the complete analysis for a sample of NPs 64 nm in width. The distribution of α is clearly wider than for the 75 nm NPs discussed in the main text (compare Figure S8b to Figure 5 of the main text). Furthermore, the pentagons often switch orientation (red to blue) in the rows, see Figure S8a. In contrast, the crystal lattice remains very well defined (compare Figure S8d to Figure 5 of the main text). This result can be attributed to the ligand corona, which tends to round the vertices and edges of the NPs and decreases the facet area that can be in contact. This effect is stronger for smaller NPs and favors the formation of plastic SCs.[S10–S12]

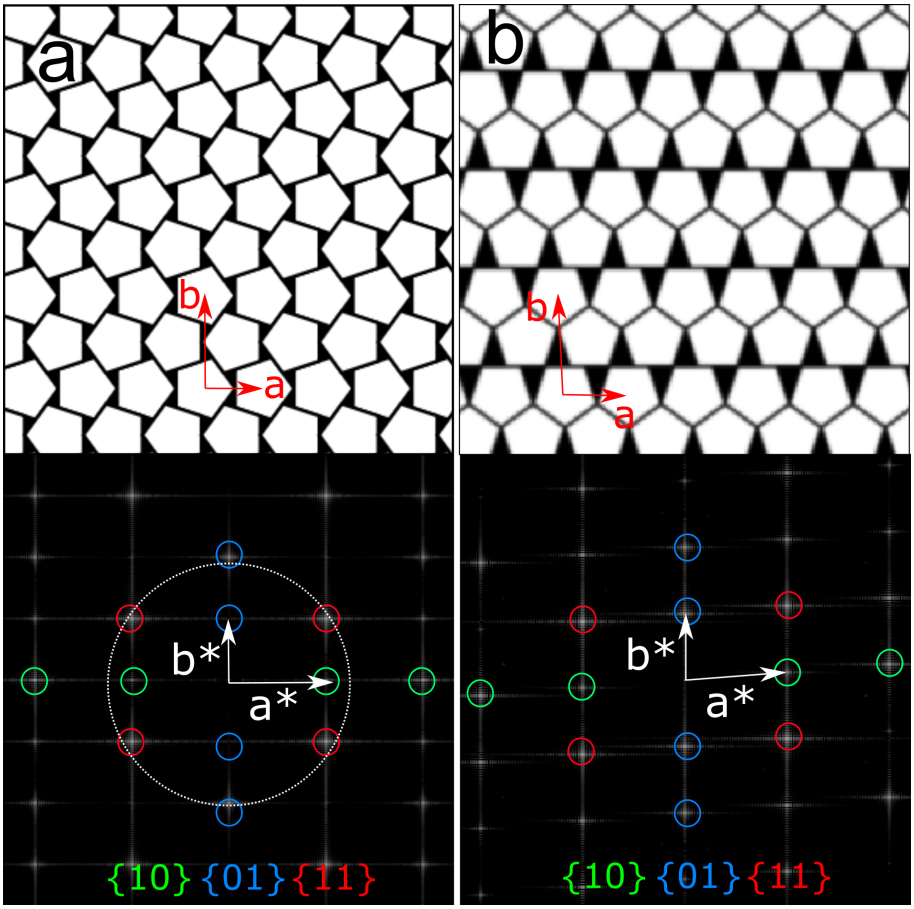

Figure S6: Comparison of the Fast Fourier Transform between the ice ray lattice and the Dürer lattice. a) top) model of a rectangular lattice (i.e. Ice-ray) of regular pentagons. bottom) corresponding FFT image;, b) top) model of a oblique lattice of regular pentagons (i.e. Dürer). bottom) corresponding FFT image. In the reciprocical space, a striking difference between the two lattices are the angle between $\mathbf{a}^*$ and $\mathbf{b}^*$ which are equals to 90° and 86.5° for the Ice-ray and Dürer lattices respectively.

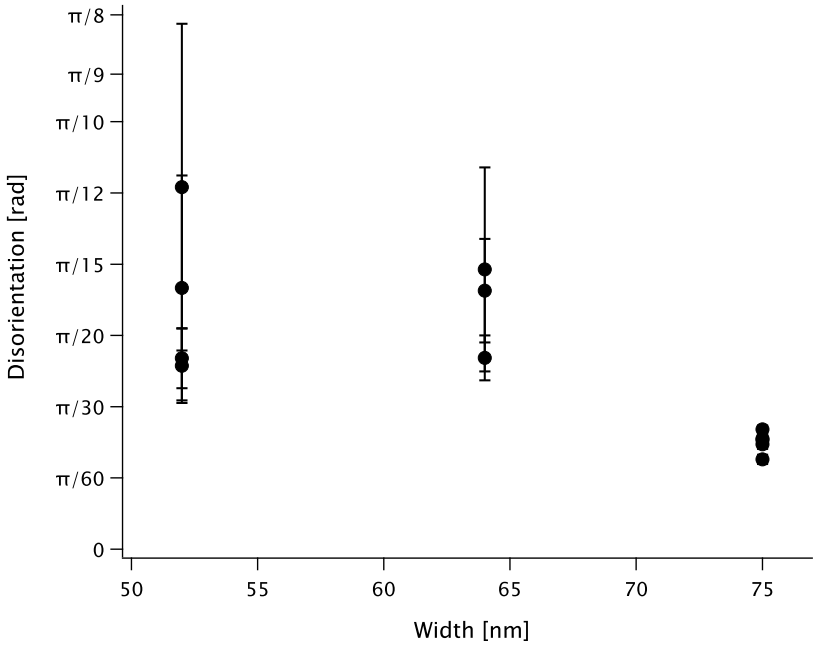

Figure S7: Disorientation as a function of the particle width. NPs-2=51.9 nm; NPs-3=64.2 nm; NPs-4=74.8 nm. Each point is obtained from the orientation distribution for one image. Error bars represent the fit uncertainty.

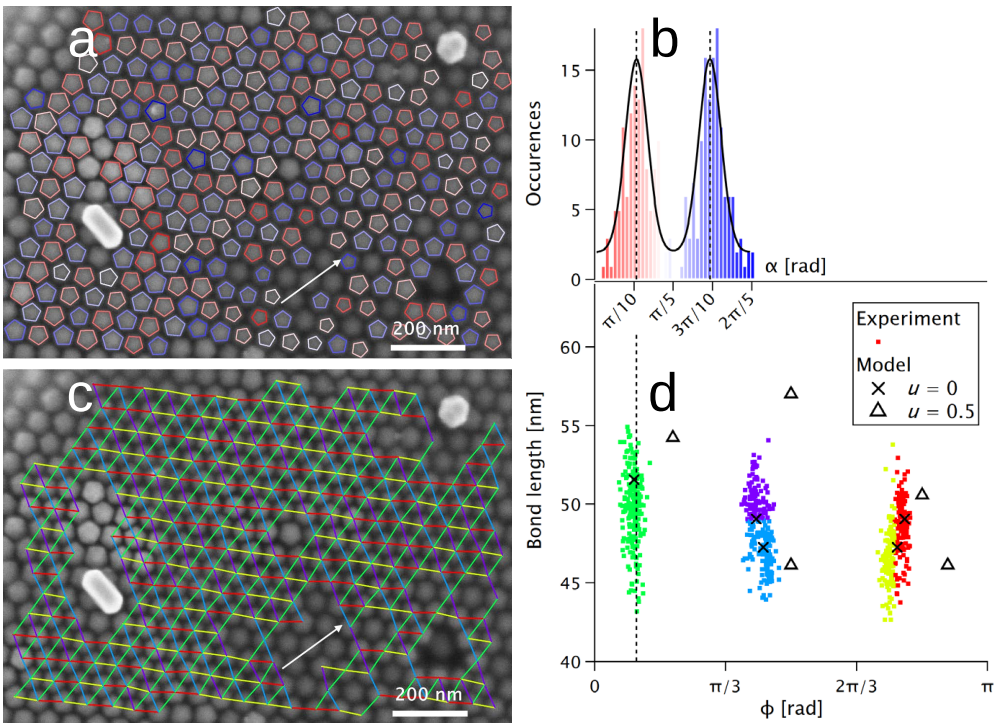

Figure S8: (a) SEM image of an SC surface, with overlaid pentagon contours (color-coded to the particle orientation angle α). (b) Histogram of the orientation angle α, with Gaussian fit. (c) As in (a), with overlaid bonds between the centers of neighboring particles (color-coded to the bond length and the bond angle ϕ). (d) Bond length plotted as a function of ϕ. The colors identify the various bond positions in the lattice.

S3 Additional SEM images

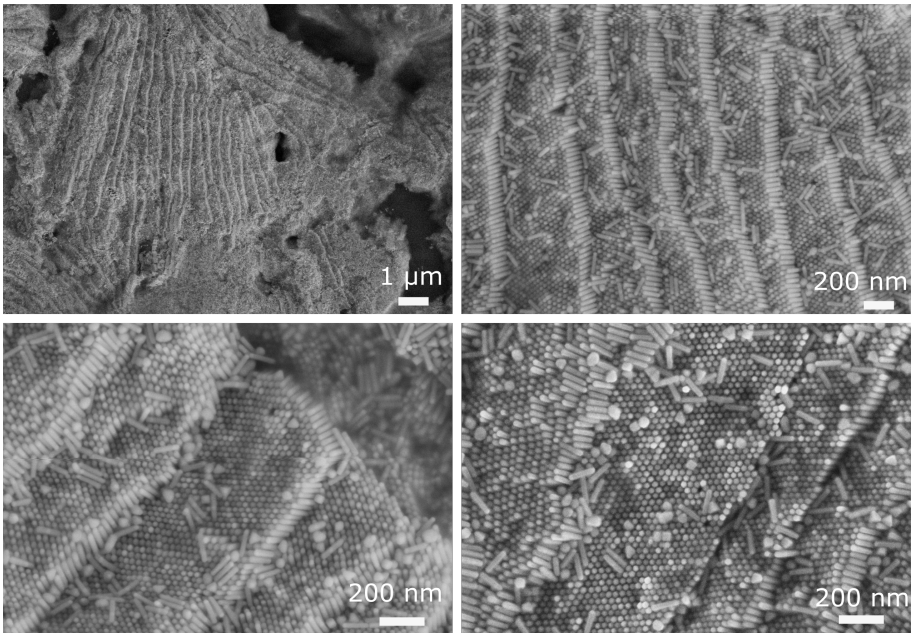

Figure S9: SEM images at different magnifications of the pentagonal NPs, obtained by drop casting. These experiments were performed with NPs-1 with 2.5 mM CTAC and 40 mM Au^0.

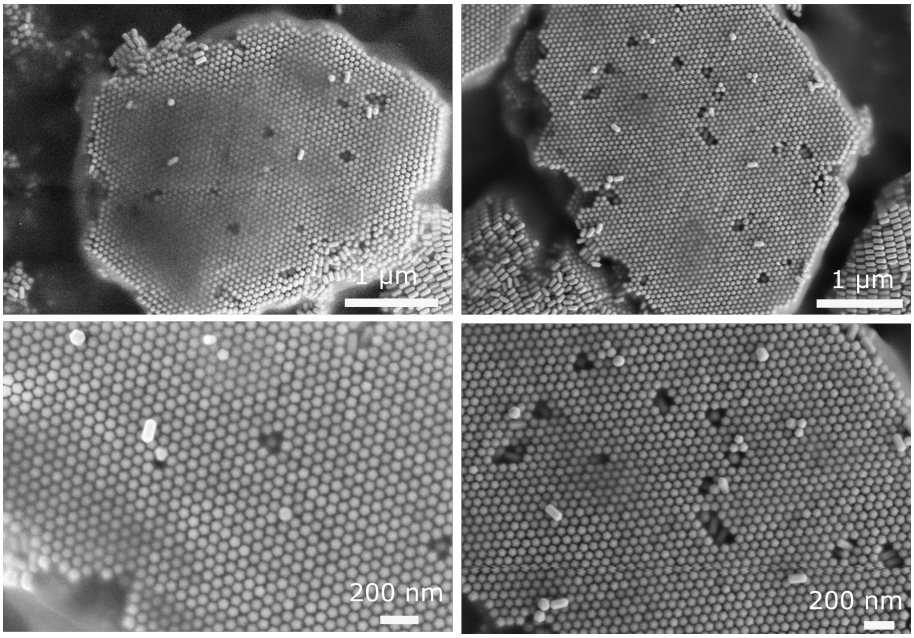

Figure S10: SEM images at different magnifications of the pentagonal NPs, obtained by drop casting. These experiments were performed with NPs-2 with 2.5 mM CTAC and 40 mM Au^0.

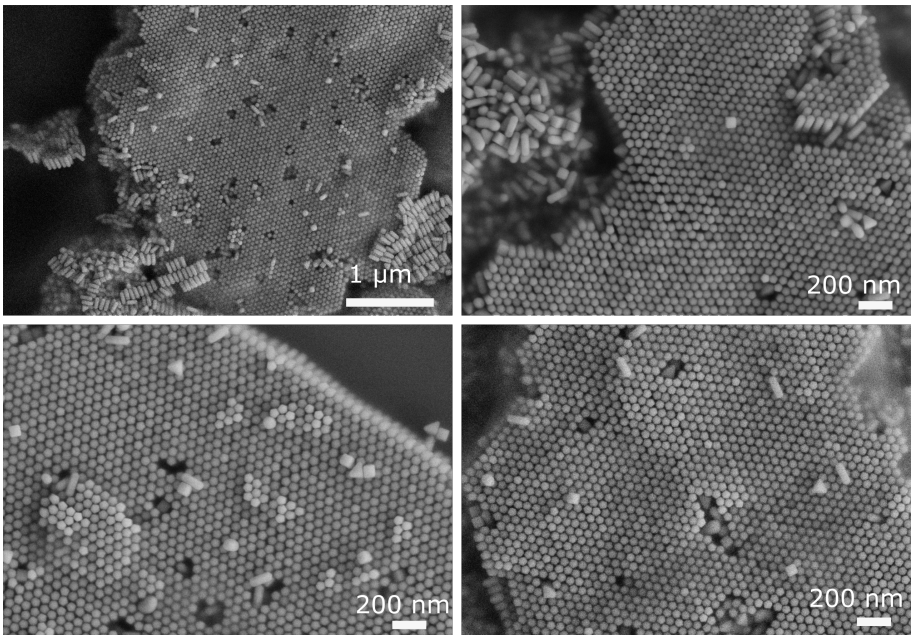

Figure S11: SEM images at different magnifications of the pentagonal NPs, obtained by drop casting. These experiments were performed with NPs-3 with 2.5 mM CTAC and 40 mM Au^0.

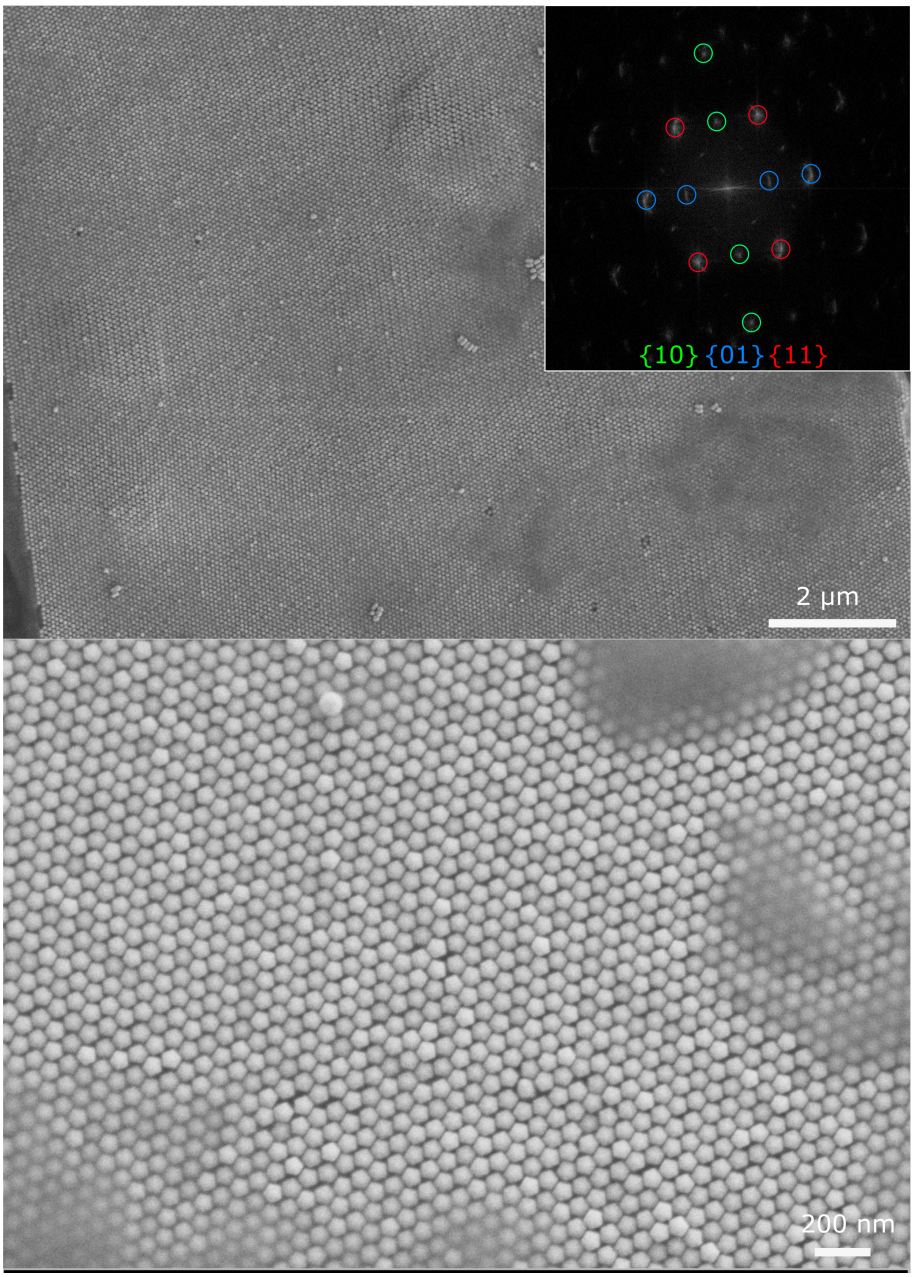

Figure S12: SEM images at different magnifications of the pentagonal NPs, obtained by drop casting. Inset is a FFT performed on the whole image, showing the extension of the lattice. These experiments were performed with NPs-4 with 2.5 mM CTAC and 40 mM Au^0.

S4 Modelling pentagonal packing

Ice-ray packing The Ice-ray packing has the maximal packing fraction of 0.921 for hard regular pentagons. The stack of alternate stripes (see Fig. S13) is the most symmetric possible one, with a mirror symmetry along a line joining centers of the pentagons in the same stripe. A rectangular unit cell $(\mathbf{a}, \mathbf{b})$ contains two pentagons in two different orientations with an inversion center I located on their common edge, at the middle point between the centers of the two pentagons. The plane space group is pm with a mirror along $\mathbf{a}$.[S13] The Ice-ray packing belongs to the family of double-lattice packing of convex bodies introduced in 1990 by G. Kuperberg and W. Kuperberg.[S14] Here the double lattice consists in the two subsets of red and blue pentagons in two different orientations which are related to each other by an inversion symmetry operation.

Coordinates are written in the complex plane with the x-axis along the $\mathbf{a}$ vector of the rectangular unit cell (see Fig. S13). The center of the pentagon in blue orientation is located at z_0 and the centers of its six nearest neighbours are located at z_1 to z_6 respectively. Here the origin is taken at $z_1 = 0$. The complex coordinates of the unit cell vectors are (z_a, z_b):

$$\begin{aligned} z_0 - z_1 &= R(\cos(\pi/5)e^{i\pi/5} + e^{2i\pi/5}) \\ z_a &= R(1 + \cos(\pi/5)) \\ z_b &= 3iR\sin(2\pi/5) \end{aligned}$$

where R is the length from the center to a vertex of a pentagon. As expected for a rectangular unit cell, z_a is a real number when z_b is an imaginary number. Position of the inversion center I is at $(z_0 + z_1)/2$, as located at the midpoint between the two pentagons centers (see Fig. S13). Note that the center of the blue pentagon is not positioned at the center of the rectangular unit cell but close to it. The bonds between centers of adjacent

pentagons are colored in five different colors depending on their orientation in the unit cell: green, cyan, red, purple and yellow. Note that the symmetry is not hexagonal but close to it, and consequently the Delaunay triangles are scalene, with three different bond lengths:

$$
\begin{aligned}
b_3 &= b_6 = R(1+\cos(\pi/5)) = 1.809R \\
b_1 &= b_5 = 1.721R \\
b_2 &= b_4 = 1.658R
\end{aligned}
$$

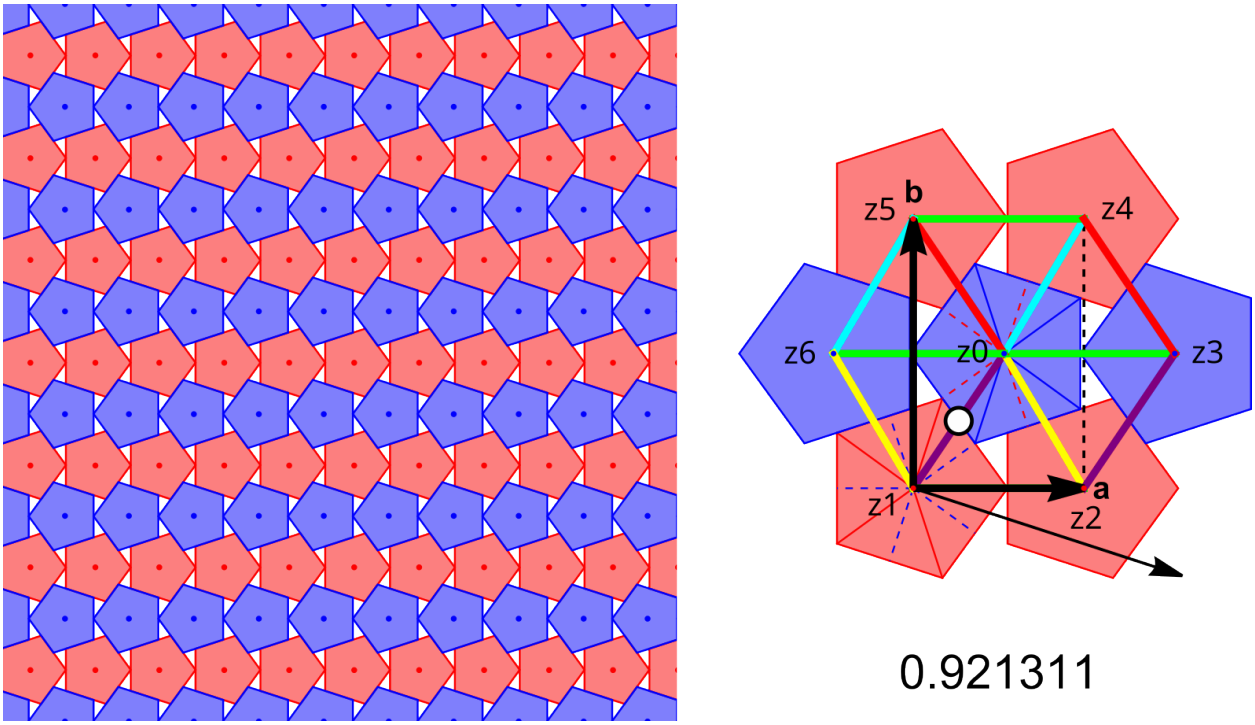

Figure S13: Ice-ray packing. The two orientations of pentagons are depicted in red and blue. (a) extended view. (b) The rectangular unit cell $(\mathbf{a}, \mathbf{b})$ with two pentagons. Position of the inversion center is depicted by a white circle.

Sliding transformation Two adjacent pentagons in two different orientations can slide along their common edge. The inversion center I moves along this edge at a position $I(u)$

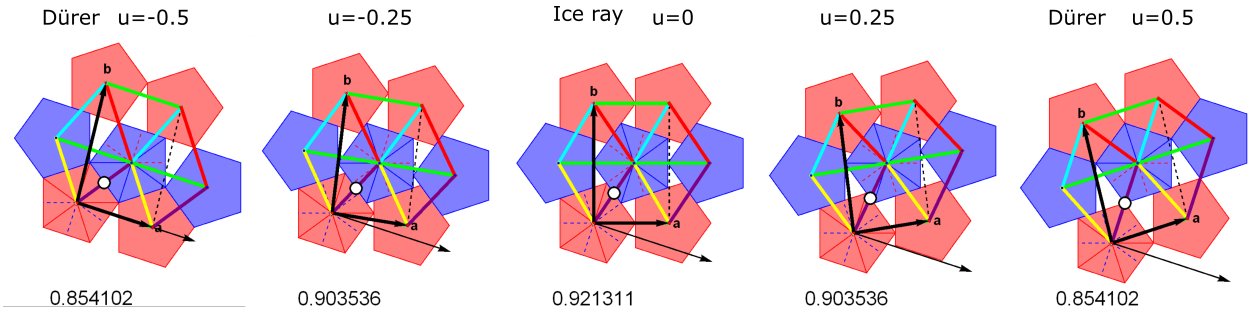

Figure S14: Sliding transformation for pentagons close packing. Value of packing fraction is given at the bottom of each unit cell.

where u is the sliding parameter which is taking values between -0.5 and $+0.5$, both values corresponding to Dürer packings when $u = 0$ corresponds to the Ice-ray one (see Fig. S14). Note that the orientation of the pentagons is still the same and the unit cell is rotated.

The unit cell becomes oblique and the plane space group is $p2$. The complex coordinates for the two unit cell vectors $z_a(u)$ and $z_b(u)$ read :

$$\begin{aligned} z_a(u) &= R(1+\cos(\pi/5)) + 2iuR\sin(\pi/5) \\ z_b(u) &= 3iR\sin(2\pi/5) + 2uR(\cos(2\pi/5) - 1) \end{aligned}$$

The position of the centers of the different pentagons are calculated depending on the sliding parameter u. Note that the pentagon with its center at z_0 is fixed. As a result, alternate

rows of blue and red pentagons are sliding along each other.

$$
\begin{aligned}
z_0 &= R(\cos(\pi/5)e^{i\pi/5} + e^{2i\pi/5}) \\
z_1(u) &= -uR(e^{2i\pi/5} - 1) \\
z_2(u) &= z_1(u) + z_a(u) \\
z_3(u) &= z_0 + z_a(u) \\
z_4(u) &= z_1(u) + z_a(u) + z_b(u) \\
z_5(u) &= z_1(u) + z_b(u) \\
z_6(u) &= z_0 - z_a(u)
\end{aligned}
$$

From these complex numbers, one can deduce all features related to the packing for any value of the sliding parameter u like the packing fraction or the lengths of the bonds between adjacent pentagons.

Finally, it is useful to figure out the sliding transformation when keeping the orientation of the lattice vector $\mathbf{a}(u)$ fixed along the x-axis, which is also the direction of the stripes. Doing so, it is easier to visualise that the orientation of the pentagons is tilted with respect to the stripes direction. This is exactly the same transformation, but a rotation has to be added to the whole figure around the center located at $z0$ using the previous notations.

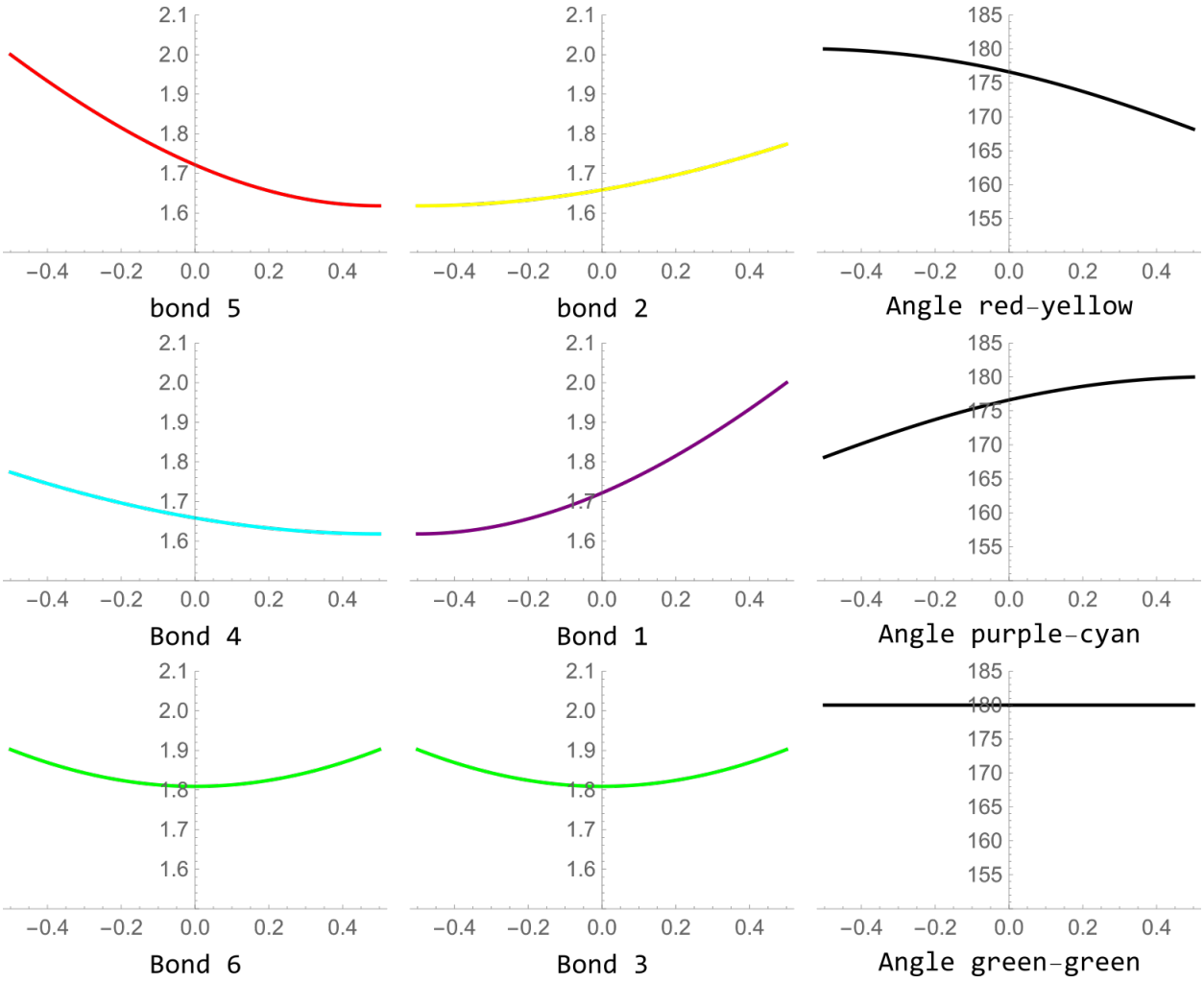

Figure S15: (left) Bond lengths (normalized by R) depending on the sliding parameter u. (right) Angle between opposite bonds depending on the sliding parameter.

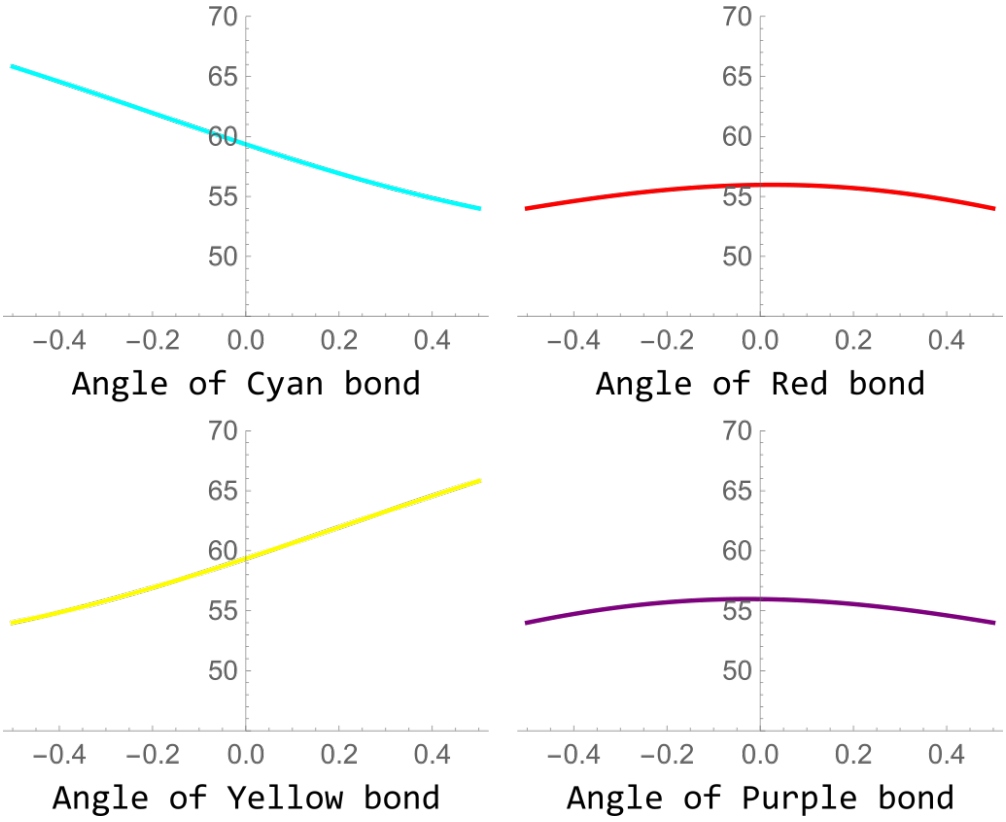

Figure S16: Angle between two bonds in a Delaunay triangle depending on the sliding parameter u. Angles are measured with respect to the green bond direction and are defined between 0° and 90°.

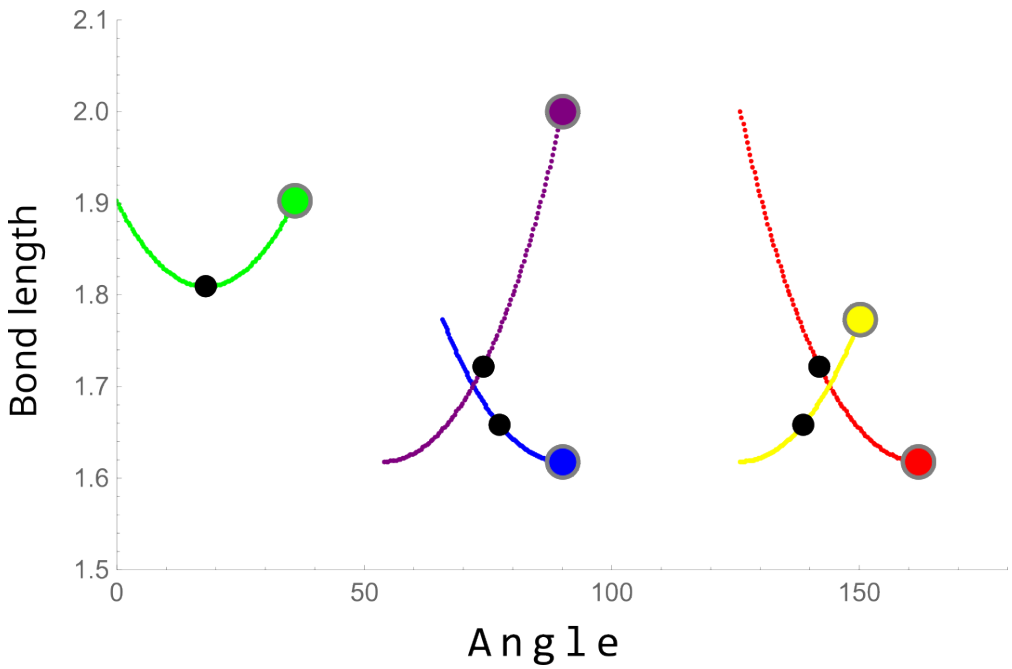

Figure S17: Bond length (normalised to R) versus angle. Black spots correspond to the Ice-ray packing for $u = 0$ and colored spots to the Dürer packing for $u = 0.5$. Colored lines correspond to all possible polymorphs for $-0.5 < u < 0.5$. Angles are defined between 0 and π.

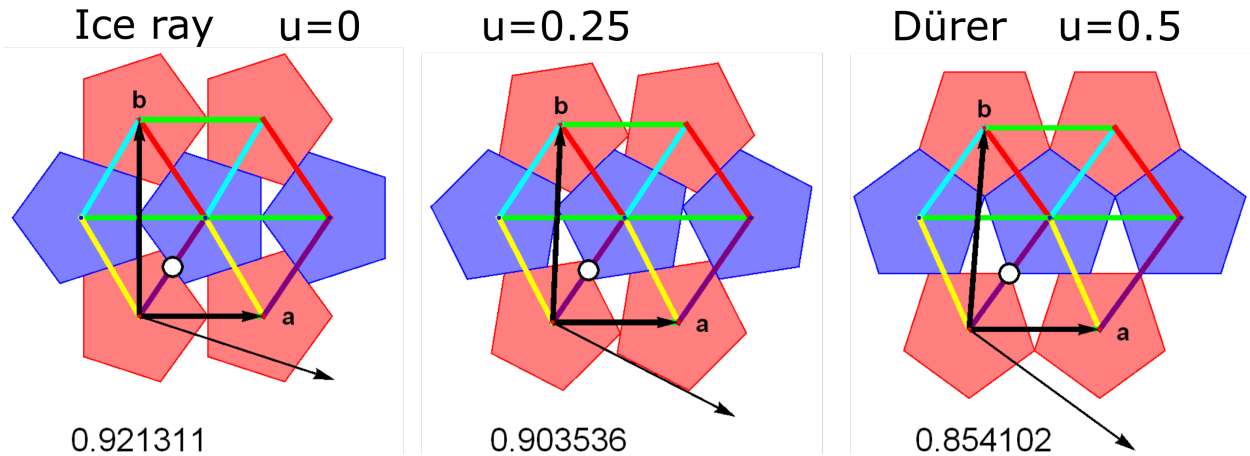

Figure S18: Sliding transformation shown for a fixed stripes direction along the lattice vector $\mathbf{a}(u)$. Note that the pentagons are tilted with respect to this direction.

References

(S1) Sánchez-Iglesias, A.; Winckelmans, N.; Altantzis, T.; Bals, S.; Grzelczak, M.; Liz-Marzán, L. M. High-Yield Seeded Growth of Monodisperse Pentatwinned Gold Nanoparticles through Thermally Induced Seed Twinning. *J. Am. Chem. Soc.* **2017**, *139*, 107–110.

(S2) Scarabelli, L.; Sánchez-Iglesias, A.; Pérez-Juste, J.; Liz-Marzán, L. M. A "Tips and Tricks" Practical Guide to the Synthesis of Gold Nanorods. *J. Phys. Chem. Lett.* **2015**, *6*, 4270–4279.

(S3) Hendel, T.; Wuithschick, M.; Kettemann, F.; Birnbaum, A.; Rademann, K.; Polte, J. In Situ Determination of Colloidal Gold Concentrations with UV–Vis Spectroscopy: Limitations and Perspectives. *Anal. Chem.* **2014**, *86*, 11115–11124.

(S4) Goldmann, C.; Li, X.; Kociak, M.; Constantin, D.; Hamon, C. Longitudinal and Transversal Directed Overgrowth of Pentatwinned Silver Nanorods with Tunable Optical Properties. *J. Phys. Chem. C* **2022**, *126*, 11667–11673.

(S5) Zhuo, X.; Zhu, X.; Li, Q.; Yang, Z.; Wang, J. Gold Nanobipyramid-Directed Growth of Length-Variable Silver Nanorods with Multipolar Plasmon Resonances. *ACS Nano* **2015**, *9*, 7523–7535.

(S6) Mayer, M.; Scarabelli, L.; March, K.; Altantzis, T.; Tebbe, M.; Kociak, M.; Bals, S.; García de Abajo, F. J.; Fery, A.; Liz-Marzán, L. M. Controlled Living Nanowire Growth: Precise Control over the Morphology and Optical Properties of AgAuAg Bimetallic Nanowires. *Nano Lett.* **2015**, *15*, 5427–5437.

(S7) Park, K.; Koerner, H.; Vaia, R. A. Depletion-Induced Shape and Size Selection of Gold Nanoparticles. *Nano Lett.* **2010**, *10*, 1433–1439.

(S8) Hamon, C.; Goldmann, C.; Constantin, D. Controlling the Symmetry of Supercrystals Formed by Plasmonic Core–Shell Nanorods with Tunable Cross-Section. *Nanoscale* **2018**, *10*, 18362–18369.

(S9) Scarabelli, L.; Hamon, C.; Liz-Marzán, L. M. Design and Fabrication of Plasmonic Nanomaterials Based on Gold Nanorod Supercrystals. *Chem. Mater.* **2017**, *29*, 15–25.

(S10) Agarwal, U.; Escobedo, F. A. Mesophase Behaviour of Polyhedral Particles. *Nat. Mater.* **2011**, *10*, 230–235.

(S11) Damasceno, P. F.; Engel, M.; Glotzer, S. C. Predictive Self-Assembly of Polyhedra into Complex Structures. *Science* **2012**, *337*, 453–457.

(S12) Boles, M. A.; Engel, M.; Talapin, D. V. Self-Assembly of Colloidal Nanocrystals: From Intricate Structures to Functional Materials. *Chem. Rev.* **2016**, *116*, 11220–11289.

(S13) Duparcmeur, Y. L.; Gervois, A.; Troadec, J. P. Dense Periodic Packings of Regular Polygons. *J. Phys. I* **1995**, *5*, 1539–1550.

(S14) Kuperberg, G.; Kuperberg, W. Double-Lattice Packings of Convex Bodies in the Plane. *Discrete & Computational Geometry* **1990**, *5*, 389–397.